Super-resolution mapping of wetland inundation from remote sensing imagery based on integration of back-propagation neural network and genetic algorithm

Linyi Li [a,*], Yun Chen [b], Tingbao Xu [c], Rui Liu [b,d], Kaifang Shi [b,d], Chang Huang [e]

[a] School of Remote Sensing and Information Engineering, Wuhan University, 129 Luoyu Road, Wuhan 430079, PR China
[b] CSIRO Land and Water Flagship, Clunies Ross Street, Canberra 2601, Australia
[c] Fenner School of Environment and Society, The Australian National University, Linnaeus Way, Canberra 2601, Australia
[d] Key laboratory of Geographic Information Science (Ministry of Education), East China Normal University, 500 Dongchuan Road, Shanghai 200241, PR China
[e] College of Urban and Environmental Sciences, Northwest University, 1 Xuefu Road, Xi'an 710127, PR China

ARTICLE INFO

ABSTRACT

Mapping the spatio-temporal characteristics of wetland inundation has an important significance to the study of wetland environment and associated flora and fauna. High temporal remote sensing imagery is widely used for this purpose with the limitations of relatively low spatial resolutions. In this study, a novel method based on integration of back-propagation neural network (BP) and genetic algorithm (GA), so-called IBPGA, is proposed for super-resolution mapping of wetland inundation (SMWI) from multispectral remote sensing imagery. The IBPGA-SMWI algorithm is developed, including the fitness function and integration search strategy. IBPGA-SMWI was evaluated using Landsat TM/ETM+ imagery from the Poyanghu wetland in China and the Macquarie Marshes in Australia. Compared with traditional SMWI methods, IBPGA-SMWI consistently achieved more accurate super-resolution mapping results in terms of visual and quantitative evaluations. In comparison with GA-SMWI, IBPGA-SMWI not only improved the accuracy of SMWI, but also accelerated the convergence speed of the algorithm. The sensitivity analysis of IBPGA-SMWI in relation to standard crossover rate, BP crossover rate and mutation rate was also carried out to discuss the algorithm performance. It is hoped that the results of this study will enhance the application of median-low resolution remote sensing imagery in wetland inundation mapping and monitoring, and ultimately support the studies of wetland environment.

© 2015 Elsevier Inc. All rights reserved.

1. Introduction

Wetlands are areas where water is the primary factor controlling the environment and associated plant and animal life (Ramsar, 2009). They are cradles of biological diversity, providing water and primary productivity upon which species of plants and animals depend for survival (Ramsar, 2009). Wetlands experience periodic flood inundation which exhibits changes in spatial distribution and temporal duration (Zhao, Stein, & Chen, 2011). Spatio-temporal characteristics of inundation have been studied using multi-spatial, multi-temporal and multispectral remote sensing imagery (Chen, Barrett, et al., 2014; Chen, Cuddy, Wang, & Merrin, 2011; Chen, Huang, Ticehurst, Merrin, & Thew, 2013; Chen, Wang, et al., 2014; Huang, Chen, & Wu, 2014b; Huang, Chen, Wu, Chen, et al., 2014; Huang, Chen, Wu, & Yu, 2012; Huang, Peng, Lang, Yeo, & McCarty, 2014; Marti-Cardona, Dolz-Ripolles, & Lopez-Martinez, 2013; Ticehurst, Chen, Karim, & Dushmanta, 2013). However, the current remote sensing systems generally do not have

high temporal and spatial resolutions at the same time (Huang, Chen, & Wu, 2014a; Li, Chen, Yu, Liu, & Huang, 2015). It is worth mentioning that the new sensor systems, specifically constellation systems such as RapidEye, are beginning to shift this paradigm. The current high temporal remote sensing imagery usually has relatively low spatial resolution (Huang, Chen, & Wu, 2014a; Li et al., 2015). The spatial resolution range of medium-low resolution remote sensing imagery here is 10 m–1000 m. The accuracy of wetland inundation mapping from high temporal remote sensing imagery is severely compromised due to spatial resolution constraints. One of the most popular methods to tackle this issue is super-resolution mapping.

Super-resolution mapping, also termed as sub-pixel mapping, is designed to obtain more sub-pixel spatial information within mixed pixels based on the spatial dependence assumption that observations close together are more alike than those that are further apart (Aplin & Atkinson, 2001; Atkinson, 1997, 2005). There are many methods developed for super-resolution mapping. Atkinson (1997) proposed a method to allocate land cover class proportions to sub-pixels based on a distance measure (proximate sub-pixels contributing more than distant ones). Verhoeye and De Wulf (2002) explored a method in

---

* Corresponding author. Tel.: +86 13545177585.
 E-mail address: lilinyi@whu.edu.cn (L. Li).

which the super-resolution mapping concept was formulated as a linear optimization problem to maximize spatial autocorrelation within an image. Atkinson (2005) presented an algorithm to exchange sub-pixels based on the swap which resulted in an increase in spatial correlation between sub-pixels. Mertens, De Baets, Verbeke, and De Wulf (2006) established a sub-pixel mapping algorithm based on spatial attraction models (SAM) to increase accuracy. As classic artificial intelligent methods, artificial neural networks (ANNs) have been applied to super-resolution mapping and obtained relatively satisfactory results (Li, Ling, Du, Feng, & Zhang, 2014; Mertens, Verbeke, Westra, & De Wulf, 2004; Quang, Atkinson, & Lewis, 2011; Zhang, Wu, Zhong, & Li, 2008). Some other well-known artificial intelligent methods, such as Markov random field (Ardila, Tolpekin, Bijker, & Stein, 2011; Kanemura, Maeda, & Ishii, 2009; Li, Du, & Ling, 2014) and particle swarm optimization (Li et al., 2015), have also proven to be useful for the purpose. However, due to the complexity and uncertainty of remote sensing imagery (Melin, Zibordi, & Berthon, 2012; Wu, Yi, & Zhang, 2009), super-resolution mapping of wetland inundation (SMWI) from remote sensing imagery is still a difficult task and needs further development. Integration of artificial intelligent methods may provide potential solutions to resolve this issue.

As classic artificial intelligent methods, ANNs are trained to learn the most appropriate sub-pixel distributions within mixed pixels in super-resolution mapping. The back-propagation (BP) algorithm is a typical and widely used algorithm to find the appropriate network weights, but the convergence of BP is confronted with locally optimal phenomenon (Zhang et al., 2008). Therefore, it is usually difficult for BP neural network to find the optimal sub-pixel distributions in super-resolution mapping. Genetic algorithm (GA) is a classic artificial intelligence method based on natural selection and genetics (Faghihi, Reinschmidt, & Kang, 2014; Van Coillie, Verbeke, & De Wulf, 2007). It has already proven to be effective in solving optimization issues encountered in many fields such as electricity industry (Ozturk & Ceylan, 2005; Suksonghong, Boonlong, & Goh, 2014; Vazhayil & Balasubramanian, 2014), chemical industry (Preechakul & Kheawhom, 2009; Qian, Sun, Zhong, & Luo, 2013; Yang & Yan, 2011), transportation (Delavar, Hajiaghaei-Keshteli, & Molla-Alizadeh-Zavardehi, 2010; Mahmoudabadi & Tavakkoli-Moghaddam, 2011; Mesbah, Sarvi, & Currie, 2011), environmental science (Oyana & Dai, 2010; Shad & Shad, 2012; Yang, Yang, Shen, & Li, 2006), economics (Acosta-Gonzalez & Fernandez-Rodriguez, 2014; Wiesinger, Sornette, & Satinover, 2013), and remote sensing (Song et al., 2012; Tong, Zhang, & Liu, 2010; Yang, 2007). SMWI is an optimization issue in essence. Therefore, the assumption of this study is that coupled with BP, GA has the potential to be applied to SMWI. The results of BP could be used as prior knowledge to be integrated into GA in the evolution process for finding optimal solutions. Compared with the standard GA method, the integration method is expected not only to improve the accuracy of SMWI, but also to accelerate the convergence speed of the algorithm.

In this study, the above assumption was tested by developing an integration method of BP and GA for SMWI (IBPGA-SMWI) from multi-spectral remote sensing imagery. The main objectives are (1) to build the IBPGA-SMWI algorithm, including the fitness function and the integration search strategy; (2) to compare the effects of IBPGA-SMWI with SAM-SMWI, BP-SMWI and GA-SMWI using Landsat TM/ETM + imagery from wetlands in China and Australia; and (3) to discuss the parameter sensitivity of IBPGA-SMWI.

2. Methods

2.1. Concept of SMWI

SMWI aims to obtain the most likely sub-pixel distributions of wetland inundation within a mixed pixel in such a way that the spatial dependence is maximized and the original proportion of inundation is maintained. The input to SMWI is a fraction image of wetland inundation where every fraction value only represents the proportion of inundation without specifying the location of inundation. The fraction image can be obtained by soft classification (Cheng, Varshney, & Arora, 2006; Hu, Xu, Zhang, Wang, & Zhang, 2013; Xu, Watanachaturaporn, Varshney, & Arora, 2005) of wetland inundation from remote sensing imagery. SMWI can be considered as the post processing of the soft classification to obtain more spatial distribution information of wetland inundation at a sub-pixel scale. Let S represent the scale factor between a mixed pixel and its sub-pixels in the fraction image. SMWI divides each mixed pixel into $S \times S$ sub-pixels. The basic principle of SMWI is shown in Fig. 1 which is a simple example with two classes representing wetland inundation and non-inundation, respectively. The fraction value in the fraction image represents the proportion of wetland inundation in a mixed pixel (Fig. 1(a)). Possible sub-pixel distributions of inundation in the central mixed pixel are shown in Fig. 1(b). Here, S equals to 3, so 9 sub-pixels in the center mixed pixel are created. The fraction value in the central mixed pixel is 33.3%, so there are 3 inundation sub-pixels and 6 non-inundation sub-pixels in this mixed pixel. Because the fraction value only represents the proportion of inundation without specifying the location of inundation, there are many different possible sub-pixel inundation distributions in the central mixed pixel. Fig. 1(c) describes the most likely sub-pixel distributions in the central mixed pixel according to the spatial dependence assumption that observations close together are more alike than those that are further apart (Aplin & Atkinson, 2001; Atkinson, 1997, 2005).

2.2. SAM-SMWI method

The SAM method is based on the fraction values in neighboring pixels acting towards sub-pixels inside a central pixel (Mertens et al., 2006). A sub-pixel is attracted only by pixels surrounding the central pixel which means that a maximum of eight neighboring pixels are considered for attraction. The inundation attraction value (IAV) and non-inundation attraction value (NAV) for a sub-pixel $p_{a,b}$ can be calculated as follows (Mertens et al., 2006):

$$IAV\left(p_{a,b}\right) = \frac{\sum_{c=1}^{N} FV(P(c))/d\left(p_{a,b}, P(c)\right)}{N} \tag{1}$$

$$NAV\left(p_{a,b}\right) = \frac{\sum_{c=1}^{N} (1 - FV(P(c)))/d\left(p_{a,b}, P(c)\right)}{N} \tag{2}$$

$$d\left(p_{a,b}, P(c)\right) = \sqrt{[a + 0.5 - S(i + 0.5)]^2 + [b + 0.5 - S(j + 0.5)]^2} \tag{3}$$

where S is the scale factor, N is the number of the neighboring pixels, $FV(P(c))$ is the inundation fraction value of the pixel $P(c)$, $d(p_{a,b}, P(c))$ is the distance between a sub-pixel $p_{a,b}$ and a neighboring pixel $P(c)$, a and b are the row and column of the sub-pixel $p_{a,b}$ in the central pixel respectively, and i and j are the row and column of the neighboring pixel $P(c)$ relative to the central pixel respectively.

If $IAV(p_{a,b}) \geq NAV(p_{a,b})$, then the sub-pixel $p_{a,b}$ is inundation. Otherwise the sub-pixel $p_{a,b}$ is non-inundation.

2.3. BP-SMWI method

ANNs are classic artificial intelligence methods, which can learn relations from examples without making assumptions about data distribution (Paola & Schowengerdt, 1995; Zhang et al., 2008). BP-SMWI constructs a local SMWI model describing the relationship between fractions in a local area and sub-pixel distributions within the central mixed pixel in the area. BP neural network consists of an input layer, an output layer and one or more hidden layers. The local area consists of 3×3 pixels including a central pixel and its eight surrounding
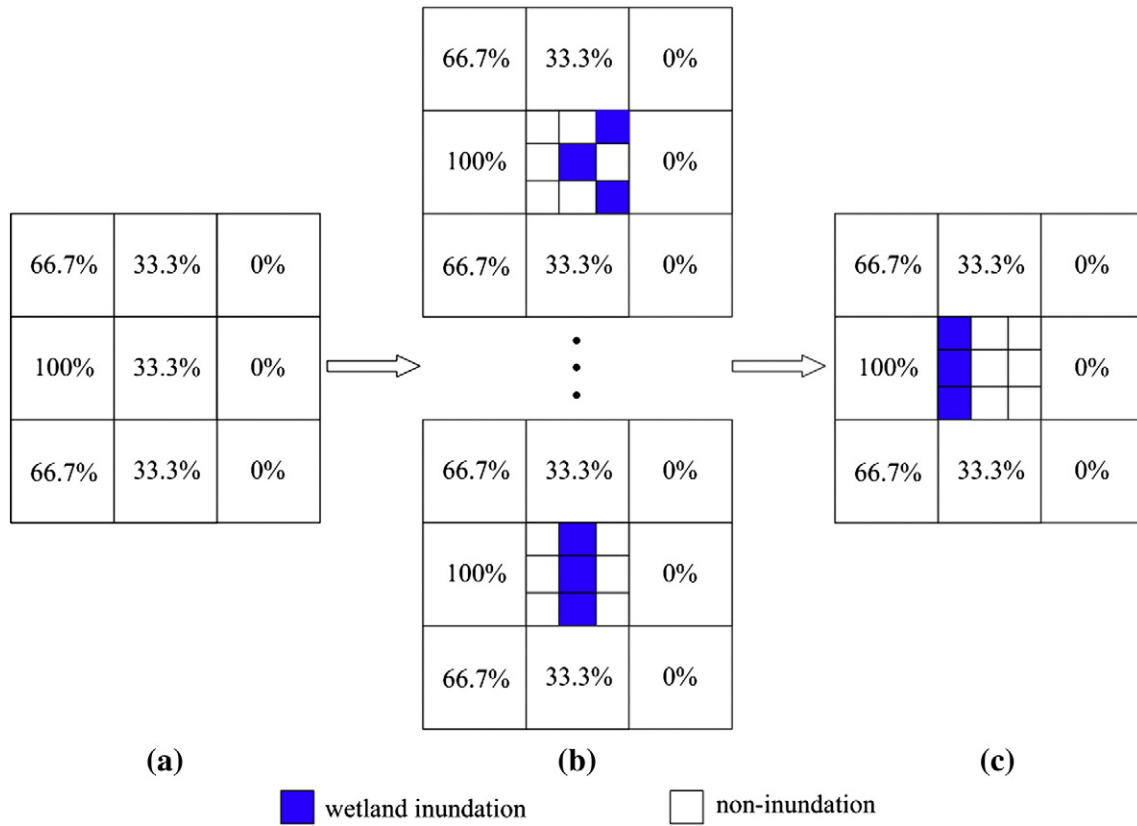
Fig. 1. An example of SMWI (S = 3). (a) Fraction image of wetland inundation. (b) Possible SMWI results. (c) The most likely SMWI result.

neighbors, so there are eight neurons in the input layer, corresponding to eight surrounding neighbors. When the scale factor S equals to 3, there are nine neurons in the output layer, corresponding to sub-pixel distributions within the central mixed pixel. The BP neural network architecture with one hidden layer is shown in Fig. 2. The BP neural network is trained to map the input samples on the correct outputs through multiple feed-forward and back-propagated phases (Zhang et al., 2008). Each input sample is first propagated through the neural network in the feed-forward phase. Then the difference between the calculated and the reference output is back-propagated from the output layer to the input layer, thereby adjusting the neural network weights in the opposite direction of the derivative of the neural network errors. However, the convergence of BP neural network is confronted with a locally optimal phenomenon in the training process (Zhang et al., 2008), which affects the results of the BP-SMWI method.

2.4. IBPGA-SMWI method

2.4.1. Basic principle of GA

The basic principle of GA is based on the Darwinian theory of evolution (Faghihi et al., 2014; Van Coillie et al., 2007). It applies the principle of survival of the fittest to find an optimal solution for optimization problems. GA deals with a population of solutions directly. Individuals spread throughout the solution space, so the chance of reaching the global optimum increases significantly. GA is also an iteration algorithm. New individuals are created through the evolutionary process of their parents according to the fitness level associated to the optimization problem. The fitness level of the individual is measured by a fitness function, which is a mathematically defined objective function. Individuals are represented as chromosomes and are randomly generated for the first generation. The evolutionary process includes three key operations, i.e. selection, crossover and mutation. Individuals are selected through a fitness-based process, where fitter individuals are more likely
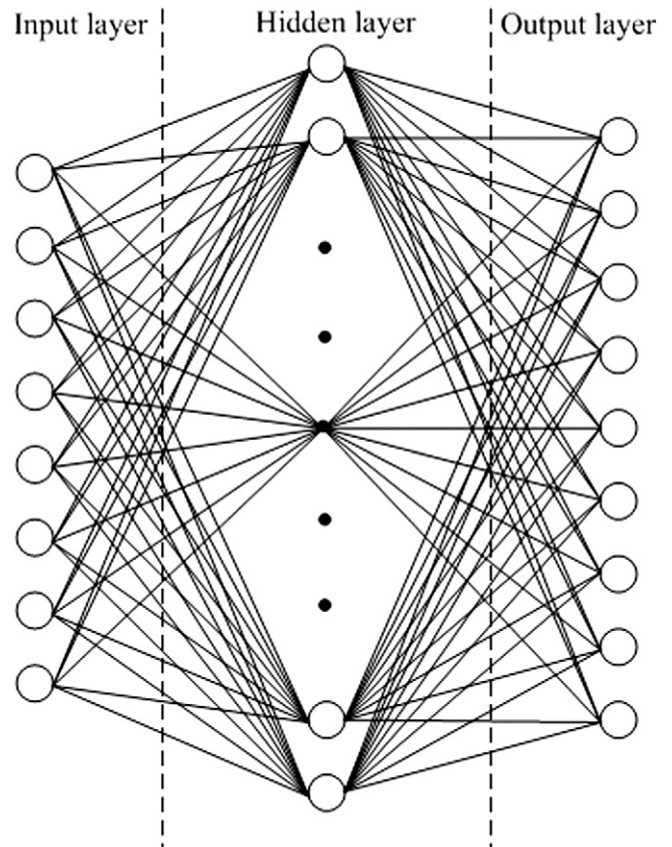

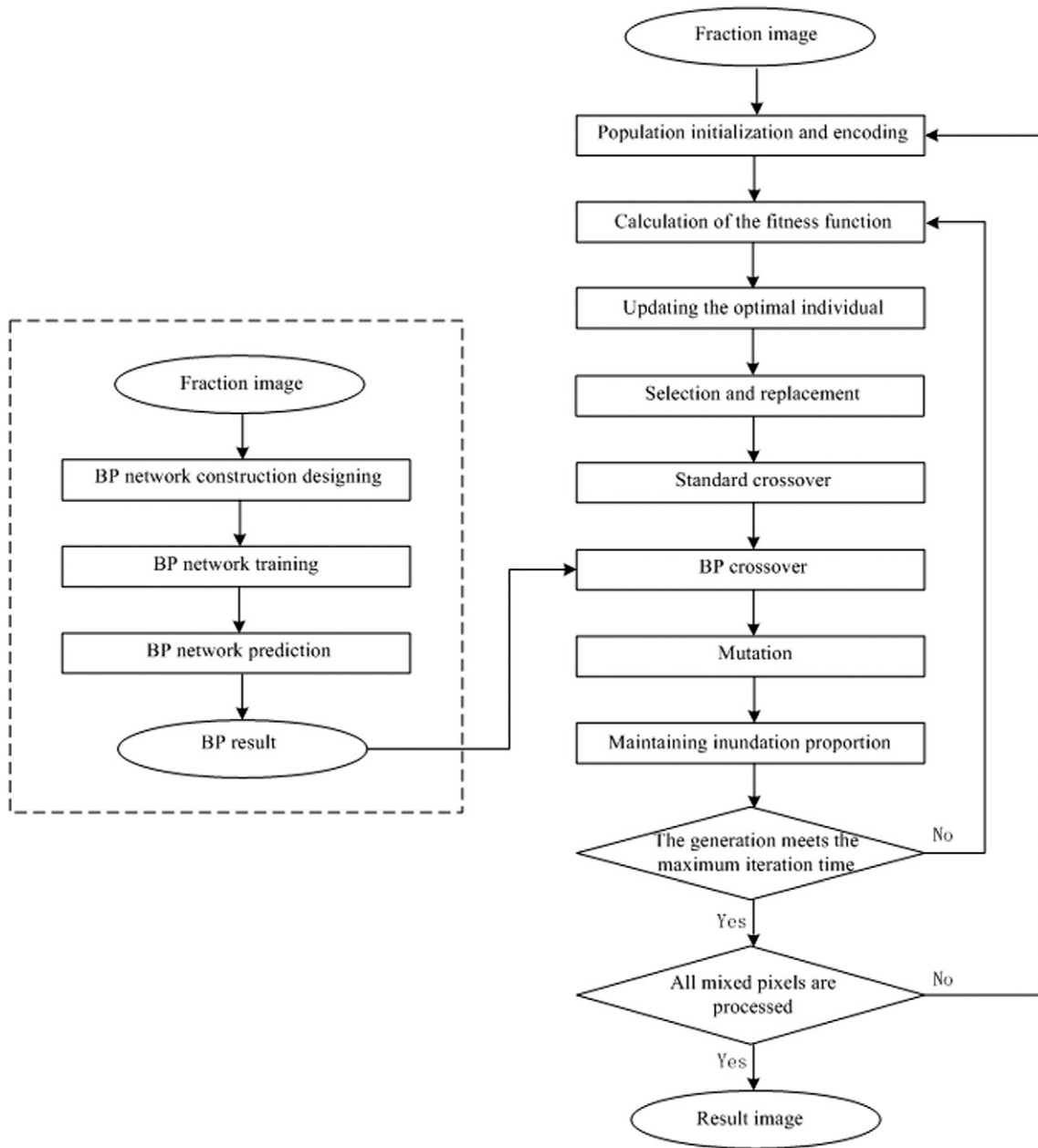**Fig. 2.** BP neural network architecture with one hidden layer (S = 3).

Fig. 3. Flow chart of IBPGA-SMWI.

to be selected. Crossover is the operation which swaps gene values between two parent individuals to breed two new individuals as their children. Mutation is used to alter the value of a gene in an individual randomly. This process leads to the evolution of more suitable generations, similar to the natural adaptation. Compared with the traditional methods which depend on existence and continuity of derivatives or other auxiliary information, GA only uses fitness information or objective function, and therefore has a wider range of applications.
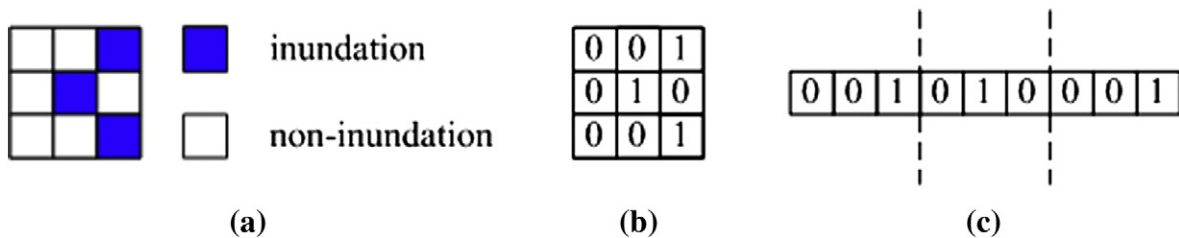

Fig. 4. An example of discrete encoding for SMWI (S = 3). (a) Possible distributions of inundation in a mixed pixel. (b) Corresponding discrete binary representation of inundation distributions. (c) Corresponding discrete encoding of the individual.
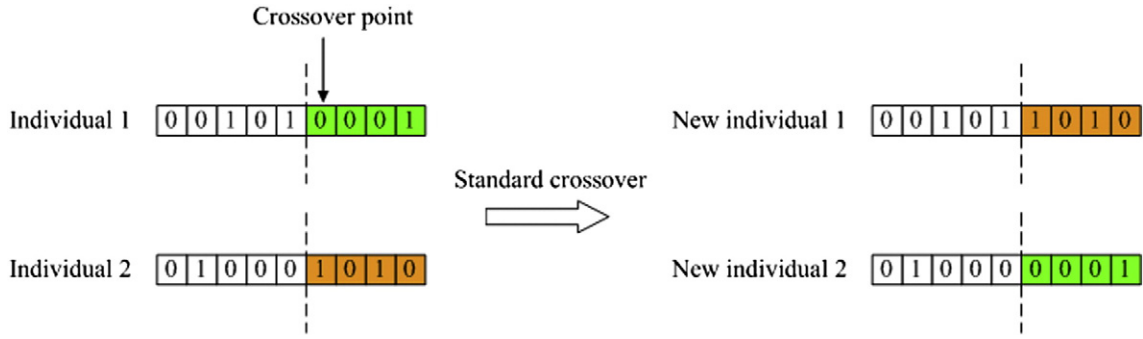
Fig. 5. A simple example of standard crossover (S = 3).

2.4.2. IBPGA-SMWI algorithm

The two key points in the development of the IBPGA-SMWI algorithm are: (1) fitness function designing and (2) integration search strategy.

(1) Fitness function designing

According to spatial dependence principles (Atkinson, 1997, 2005), SMWI can be formulated as a maximum combined optimization issue. For a mixed pixel, the wetland inundation spatial dependence index (WISDI) can be calculated considering the spatial correlation between its sub-pixels and neighboring mixed pixels:

$$WISDI = \sum_{i=1}^{S*S} WISDI_i \tag{4}$$

$$WISDI_i = b_i \cdot \left(\sum_{j=1}^{J} w_j \cdot fraction_j \right) + (1 - b_i) \cdot \left[\sum_{j=1}^{J} w_j \cdot \left(1 - fraction_j \right) \right] \tag{5}$$

where S represents the scale factor which refers to the scale ratio between the mixed pixel and its sub-pixels, b_i is the binary class of each sub-pixel i (1 for the inundation class and 0 for the non-inundation class), J is the number of the neighboring mixed pixels, w_j is usually calculated as the distance inverse of each sub-pixel i to the jth neighboring mixed pixel center, and $fraction_j$ is the wetland inundation fraction value of the jth neighboring mixed pixel.

The evaluation criterion of SMWI can be formulated as: the higher the WISDI value, the higher the possibility of the sub-pixel distributions. Therefore, SMWI spatially allocates wetland inundation to the sub-pixels in a mixed pixel while maximizing the WISDI.

Fitness function value is a measure of an individual. If an individual has a larger fitness function value, the distributions of inundation represented by the individual are more likely. The fitness function for SMWI can be defined as follows:

$$FitnessFunction_i = WISDI(Individual_i) \tag{6}$$

where $FitnessFunction_i$ is the fitness function of the ith individual, and $WISDI$ is the spatial dependence index of the ith individual.

(2) Integration search strategy

A flow chart of IBPGA-SMWI is shown in Fig. 3.

For each mixed pixel in the fraction image, the integration search strategy is described below.

(a) Population initialization and discrete encoding

Each individual $G_i(g_{i1}, g_{i2} \cdots, g_{iM})$ represents a possible solution of SMWI, where M is equal to $S * S$. The basic principle of the discrete encoding for SMWI is illustrated in Fig. 4. Possible distributions of wetland inundation in a mixed pixel are depicted in Fig. 4(a). The corresponding binary representation of inundation distributions is in Fig. 4(b), where inundation is represented by 1 and non-inundation is represented by 0. Fig. 4(c) shows the corresponding discrete encoding of the individual by placing each row in Fig. 4(b) end to end.

All individuals of the population compose a matrix G as follows:

$$G = \begin{bmatrix} G_1 \\ G_2 \\ \vdots \\ G_N \end{bmatrix} = \begin{bmatrix} g_{11} & g_{12} & \cdots & g_{1M} \\ g_{21} & g_{22} & \cdots & g_{2M} \\ \vdots & \vdots & \vdots & \vdots \\ g_{N1} & g_{N2} & \cdots & g_{NM} \end{bmatrix} \tag{7}$$

where g_{im} represents a gene ($1 \leq i \leq N$, $1 \leq m \leq M$), $G = _i[g_{i1} \quad g_{i2} \quad \cdots \quad g_{iM}]$, N is the number of individuals of the population, and M is the dimension of each individual.

The population matrix G is initialized according to Eq. (7), where the elements are initialized according to the following equations:
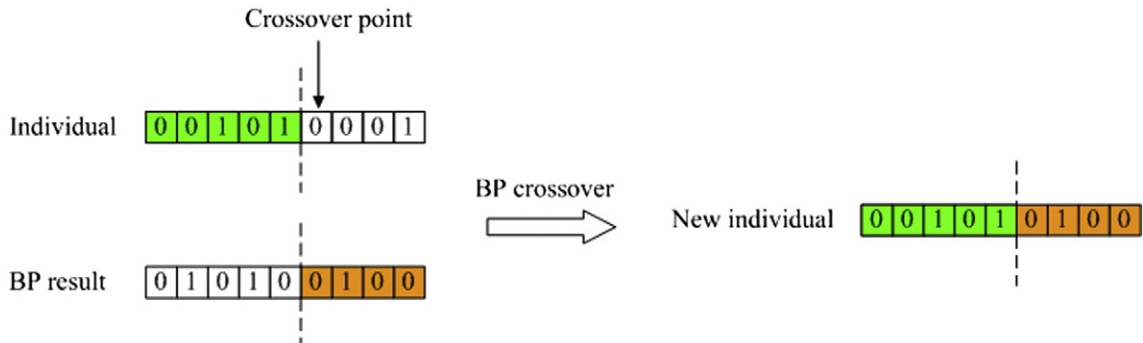
$$g_{im} = rand\,int() \tag{8}$$

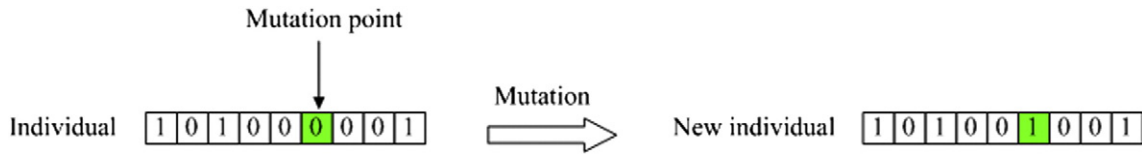**Fig. 6.** A simple example of BP crossover (S = 3).

Fig. 7. A simple example of mutation (S = 3).

$$\sum_{m=1}^{M} g_{im} = Fraction = fraction \times S^2 \tag{9}$$

where $rand\ int()$ is the random number with the value of '0' or '1', and $fraction$ is the fraction value of wetland inundation of the mixed pixel.

(b) Calculation of the fitness function

The fitness of each individual is measured by the fitness function in SMWI:

$$FitnessFunction_i = WISDI(g_{i1}, g_{i1}, \cdots, g_{iM}) \tag{10}$$

where $FitnessFunction_i$ is the fitness function of the ith individual $(g_{i1}, g_{i1}, \cdots, g_{iM})$, and $WISDI$ is its corresponding spatial dependence index when inundation distributions in a mixed pixel are represented by the ith individual.

(c) Updating the optimal individual (G_b)

This step updates the optimal individual of the population. Compare the evaluated fitness value of each current individual with the fitness value of the optimal individual G_b in the history of the whole population. If the current value is better, then set the current individual as G_b.

(d) Selection and replacement

The individuals are firstly ranked based on their fitness values. Those individuals that have higher fitness values are ranked higher and those with lower fitness values have lower ranks. Then the individuals are selected according to their ranks. Those individuals that have low ranks are replaced by those have high ranks.

(e) Standard crossover

Standard crossover swaps gene values between two individuals so as to generate two new individuals. The standard crossover rate is the probability of the individuals participating in the standard crossover process. The individuals are randomly selected according to the standard crossover rate. A simple example of standard crossover is shown in Fig. 5 where the crossover point is randomly generated within the integer domains 1 to 9. The crossover attaches the first part of individual 1 to the second part of individual 2 to generate new individual 1. And it attaches the first part of individual 2 to the second part of individual 1 to generate new individual 2.

(f) BP crossover

The results of the BP method can be used as prior knowledge and integrated into the GA evolution process by BP crossover. The BP crossover rate is the probability of the individuals participating in the BP crossover process. The individuals are randomly selected according to the BP crossover rate. BP crossover swaps gene values between the individual and BP result so as to generate a new individual. A simple example of BP crossover is shown in Fig. 6 where the crossover point is randomly generated within the integer domains 1 to 9. The crossover attaches the first part of the individual to the second part of BP result to generate a new individual. Compare the fitness value of the new individual with the fitness value of the previous one. If the fitness value of the new individual is higher, then replace the previous individual with the new one.

(g) Mutation

Mutation is to alter the binary value of a gene in an individual randomly. The mutation rate is the probability of the individuals participating in the mutation process. The individuals are randomly selected according to the mutation rate. A simple example of mutation is shown in Fig. 7 where the mutation point is randomly generated within the integer domain 1 to 9. Here the value of a gene at the mutation point is changed from 0 to 1.

(h) Maintaining the original proportion of inundation

This step maintains the original proportion of inundation. If $\sum_{m=1}^{M} g_{im} > Fraction$, then compare each individual with G_b, and retain genes in common whose value is equal to 1. Randomly change the value of other genes whose value is equal to 1 to satisfy $\sum_{m=1}^{M} g_{im} > Fraction$. If $\sum_{m=1}^{M} g_{im} > Fraction$, randomly change the value of genes whose value is equal to 0 to satisfy $\sum_{m=1}^{M} g_{im} > Fraction$.

(i) Termination conditions

If the generation meets the maximum iteration time, the loop is terminated. The output is the optimal individual G_b which represents the optimal distributions of wetland inundation in a mixed pixel. Otherwise, go to step (b).

3. Materials of case study

Two comparative study areas were selected from two wetlands of international importance. The first wetland is Poyanghu, which is located in Jiangxi, China and was included in the Ramsar List on March 31, 1992 (Ramsar, 2014). The second wetland is Macquarie Marshes, which is located in New South Wales, Australia and was included in the Ramsar List on August 1, 1986 (Ramsar, 2014). The Landsat TM/ETM + images were acquired when there were significant flood events in the wetlands. These images are the L1T products, which provide systematic radiometric and geometric accuracy. In order to analyze and compare the performance of SMWI methods comprehensively, study areas with different size were selected: one small area from Poyanghu and one large area from Macquarie Marshes, respectively. Key characteristics of the two study sites are summarized in Table 1.

Locations of the study areas are shown in color composite (R5G2B1) Landsat images in Fig. 8(a) and (d) respectively. The reference images (Fig. 8(b) and (e)) were derived from the corresponding Landsat images at 30 m resolution using the modified normalized difference water index (mNDWI; Xu, 2006). The mNDWI was calculated according to the following equation (Xu, 2006):

$$mNDWI = (Green - SWIR)/(Green + SWIR) \tag{11}$$

Table 1
Key characteristics of the two study areas.

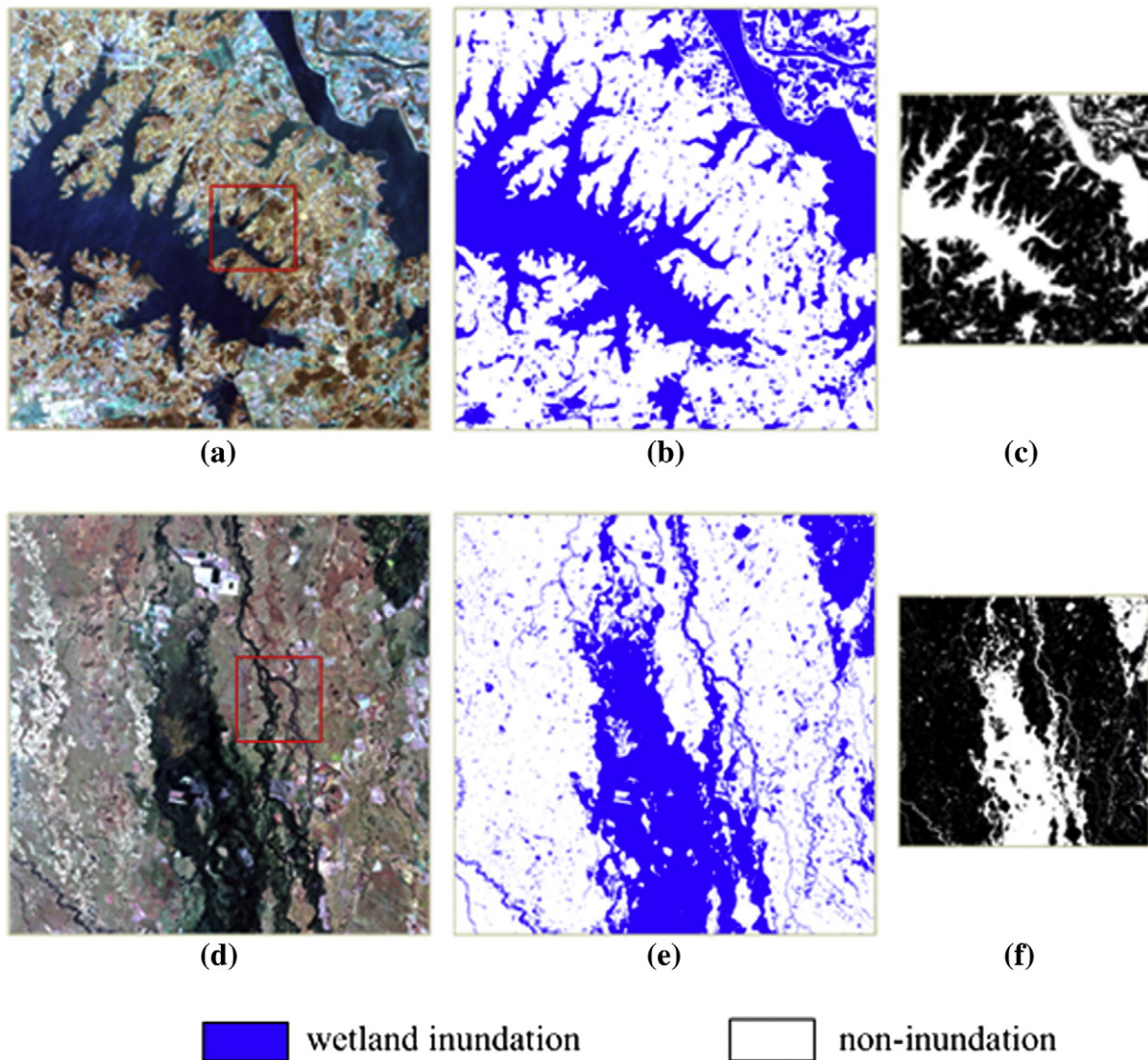|	Study area 1	Study area 2
Location	Poyanghu, Jiangxi, China	Macquarie Marshes, New South Wales, Australia
Area	225 km^2	5625 km^2
Data	A Landsat 7 ETM+ image	A Landsat 5 TM image
Date	August 2, 2010	December 20, 2010
Image size	500 × 500 pixels	2500 × 2500 pixels
Image resolution	30 m	30 m

Fig. 8. Materials of the two comparative study areas. (a) Location of the study area 1 shown in a color composite (R5G2B1) Landsat 7 ETM+ image (500 × 500 pixels) at 30 m resolution after image enhancement. (b) Inundation reference image (500 × 500 pixels) at 30 m resolution. (c) Inundation fraction image (100 × 100 pixels) at 150 m resolution. (d) Location of the study area 2 shown in a color composite (R5G2B1) Landsat 5 TM image (2500 × 2500 pixels) at 30 m resolution after image enhancement. (e) Inundation reference image (2500 × 2500 pixels) at 30 m resolution. (f) Inundation fraction image (500 × 500 pixels) at 150 m resolution.

where *Green* is the Green band (band 2 of the Landsat TM/ETM+ images), and *SWIR* is the Short-Wave Infrared band (band 5 of the Landsat TM/ETM+ images). A threshold value was used to convert the mNDWI values into a reference image which was an inundation classification result. The threshold value was set at 0 in the study area 1 and was set at −0.4 in the study area 2 by visual interpretation, respectively. In this case, the scale factor was set at 5. The inundation fraction images (Fig. 8(c) and (f)) were derived by aggregating the corresponding inundation reference images. The aggregated pixel value is equal to the proportion of inundation pixels inside a 5 × 5 window. Therefore, the resolution of the fraction images is 150 m. By simulating 150 m resolution fraction images using 30 m TM/ETM+ binary classification results, we can focus on the algorithm comparison by avoiding the need to validate the real-world inundation mapping accuracies of the study areas. The inundation fraction images were used as the inputs of the four SMWI methods.

The four SMWI methods for comparison in the study are SAM-SMWI, BP-SMWI, GA-SMWI and IBPGA-SMWI. The inputs to these methods were the same wetland inundation fraction images. The same surrounding neighboring type was used for all the methods. The back-propagation training algorithm of BP-SMWI was based on Bayesian regulation. Due to

the difference of area size, the number of mixed pixels in the study area 1 is much smaller than that in the study area 2. In order to train the BP network sufficiently, 20% mixed pixels were randomly selected as training

Table 2
Parameters of different methods.

Method	Parameter description	Parameter value
SAM-SMWI	None	None
BP-SMWI	Number of hidden layers	1
	Marquardt adjustment parameter (MAP)	0.005
	Decrease factor for MAP	0.1
	Increase factor for MAP	10
GA-SMWI	Standard crossover rate	0.5
	Mutation rate	0.5
	Size of the population	10
	Maximum iterative time	10
IBPGA-SMWI	Standard crossover rate	0.5
	BP crossover rate	0.5
	Mutation rate	0.5
	Size of the population	10
	Maximum iterative time	10

wetland inundation   non-inundation

Fig. 9. Visual comparisons of the four SMWI methods in the study area 1 (500 × 500 pixels). (a) Inundation reference image. (b) SAM-SMWI. (c) BP-SMWI. (d) GA-SMWI. (e) IBPGA-SMWI.
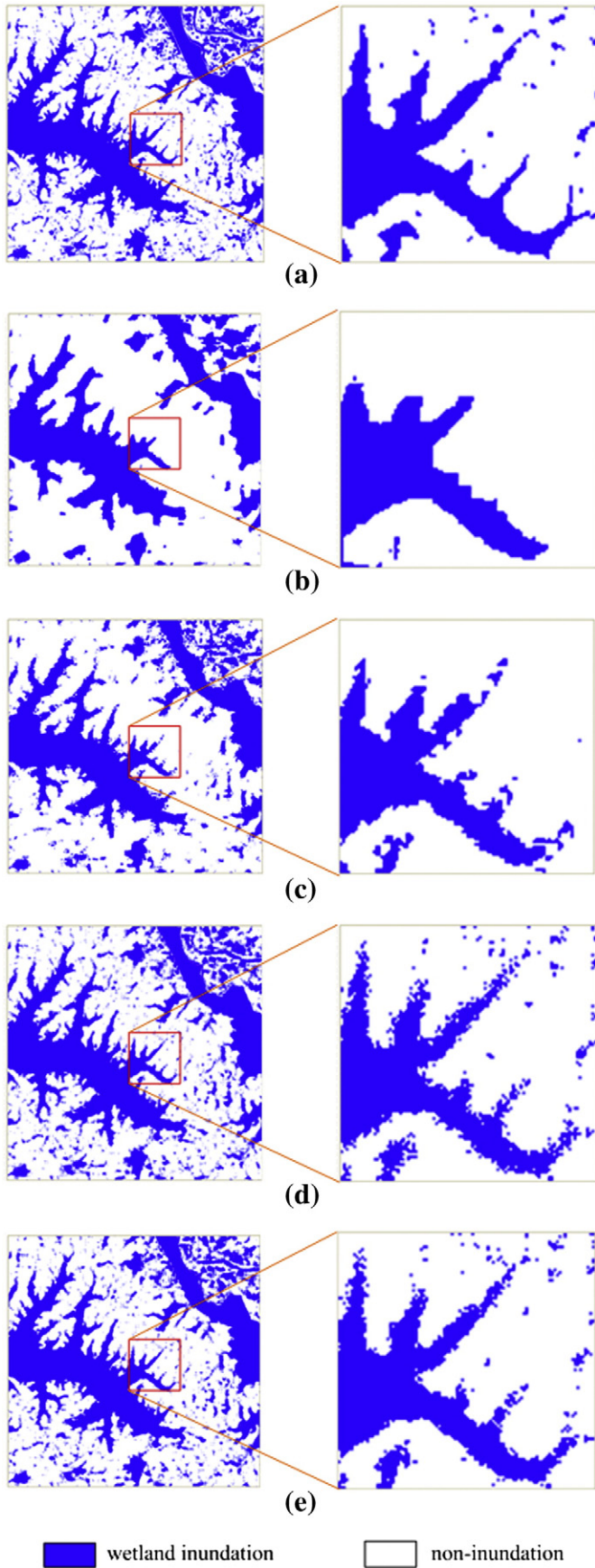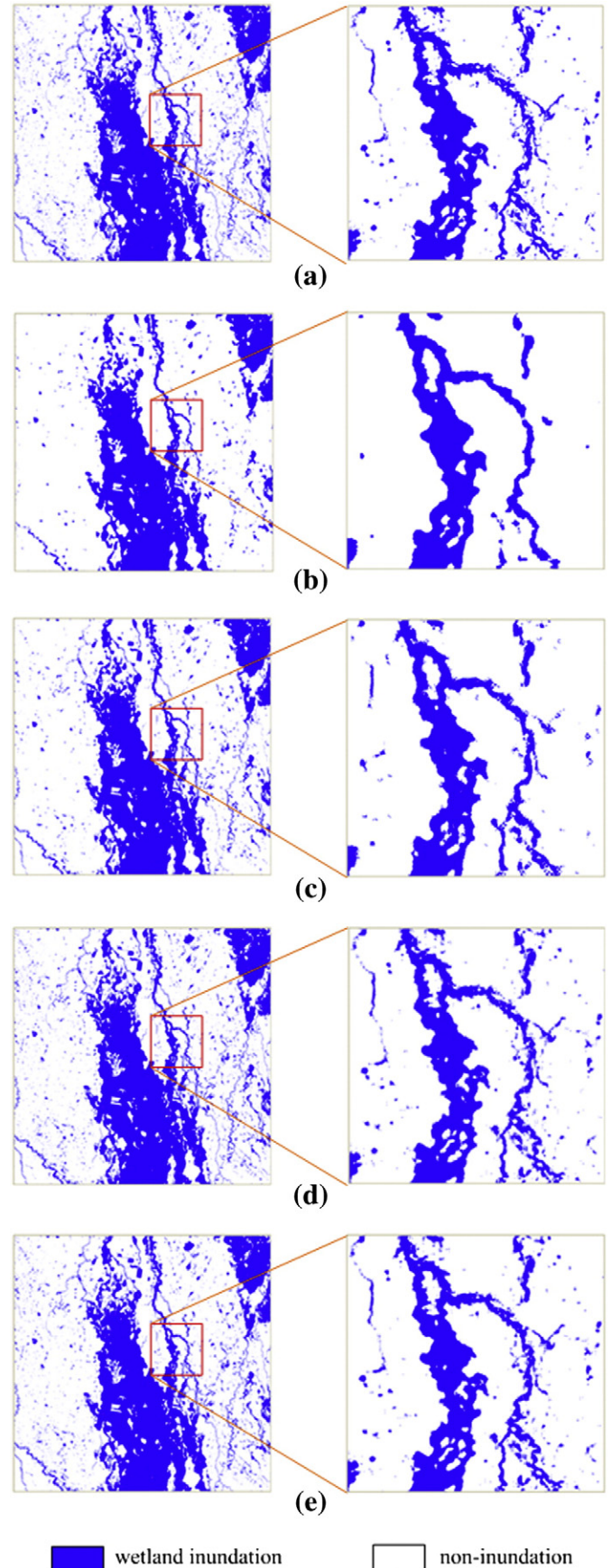
Fig. 10. Visual comparisons of the four SMWI methods in the study area 2 (2500 × 2500 pixels). (a) Inundation reference image. (b) SAM-SMWI. (c) BP-SMWI. (d) GA-SMWI. (e) IBPGA-SMWI.

Table 3
Quantitative comparisons of the four SMWI methods.

Index	Study area 1 (500 × 500 pixels)				Study area 2 (2500 × 2500 pixels)			
	SAM	BP	GA	IBPGA	SAM	BP	GA	IBPGA
OA (%)	72.4	75.4	78.5	80.1	74.1	77.8	79.3	81.0
Kappa	0.375	0.456	0.541	0.576	0.439	0.532	0.569	0.606
APA (%)	67.7	72.0	77.0	78.8	71.0	76.2	78.5	80.3
AUA (%)	71.2	74.3	77.0	78.8	74.2	77.3	78.5	80.3

Table 4
Convergence performance of GA-SMWI and IBPGA-SMWI in the study area 1. The bold data are the accuracy values of GA-SMWI at the 20th iteration and the accuracy values of IBPGA-SMWI at the 10th iteration, respectively.

ITs	GA				IBPGA			
	OA (%)	Kappa	APA (%)	AUA (%)	OA (%)	Kappa	APA (%)	AUA (%)
2	74.8	0.462	73.1	73.1	76.9	0.507	75.3	75.3
4	75.9	0.486	74.3	74.3	78.7	0.546	77.3	77.3
6	76.9	0.508	75.4	75.4	79.2	0.556	77.8	77.8
8	77.6	0.522	76.1	76.1	79.7	0.568	78.4	78.4
10	78.5	0.541	77.0	77.0	**80.1**	**0.576**	**78.8**	**78.8**
12	78.9	0.550	77.5	77.5	80.3	0.580	79.0	79.0
14	79.1	0.555	77.7	77.7	80.4	0.582	79.1	79.1
16	79.5	0.562	78.1	78.1	80.7	0.588	79.4	79.4
18	79.8	0.570	78.5	78.5	80.8	0.590	79.5	79.5
20	**79.9**	**0.573**	**78.6**	**78.6**	80.9	0.594	79.7	79.7

samples in the study area 1 and 5% mixed pixels were randomly selected as training samples in the study area 2, respectively. The parameters of different methods are shown in Table 2.

Table 5
Sensitivity of IBPGA-SMWI.

Parameter		Study area 1				Study area 2			
		OA (%)	Kappa	APA (%)	AUA (%)	OA (%)	Kappa	APA (%)	AUA (%)
SCR	0.1	79.7	0.568	78.4	78.4	82.1	0.635	81.7	81.7
	0.3	80.0	0.574	78.7	78.7	82.2	0.636	81.8	81.8
	0.5	80.1	0.576	78.8	78.8	82.5	0.643	82.2	82.2
	0.7	80.1	0.576	78.8	78.8	82.6	0.644	82.2	82.2
	0.9	80.2	0.577	78.9	78.9	82.8	0.649	82.5	82.5
BPCR	0.1	79.5	0.564	78.2	78.2	81.9	0.629	81.5	81.5
	0.3	80.0	0.574	78.7	78.7	82.3	0.638	81.9	81.9
	0.5	80.1	0.576	78.8	78.8	82.5	0.643	82.2	82.2
	0.7	80.0	0.574	78.7	78.7	82.4	0.641	82.0	82.0
	0.9	79.9	0.572	78.6	78.6	82.3	0.638	81.9	81.9
MR	0.1	79.4	0.561	78.0	78.0	81.7	0.625	81.3	81.3
	0.3	79.6	0.566	78.3	78.3	82.2	0.636	81.8	81.8
	0.5	80.1	0.576	78.8	78.8	82.5	0.643	82.2	82.2
	0.7	80.2	0.578	78.9	78.9	82.7	0.647	82.4	82.4
	0.9	80.3	0.580	79.0	79.0	82.8	0.648	82.4	82.4

4. Results and discussion

4.1. Comparative analysis of four SMWI methods

Visual comparisons of the four SMWI methods in the two study areas are shown in Figs. 9 and 10 respectively. The same small regions from both reference and result images were zoomed to enhance the clarity. As shown in Figs. 9 and 10, GA-SMWI performed better than SAM-SMWI and BP-SMWI, because the results of GA-SMWI are more
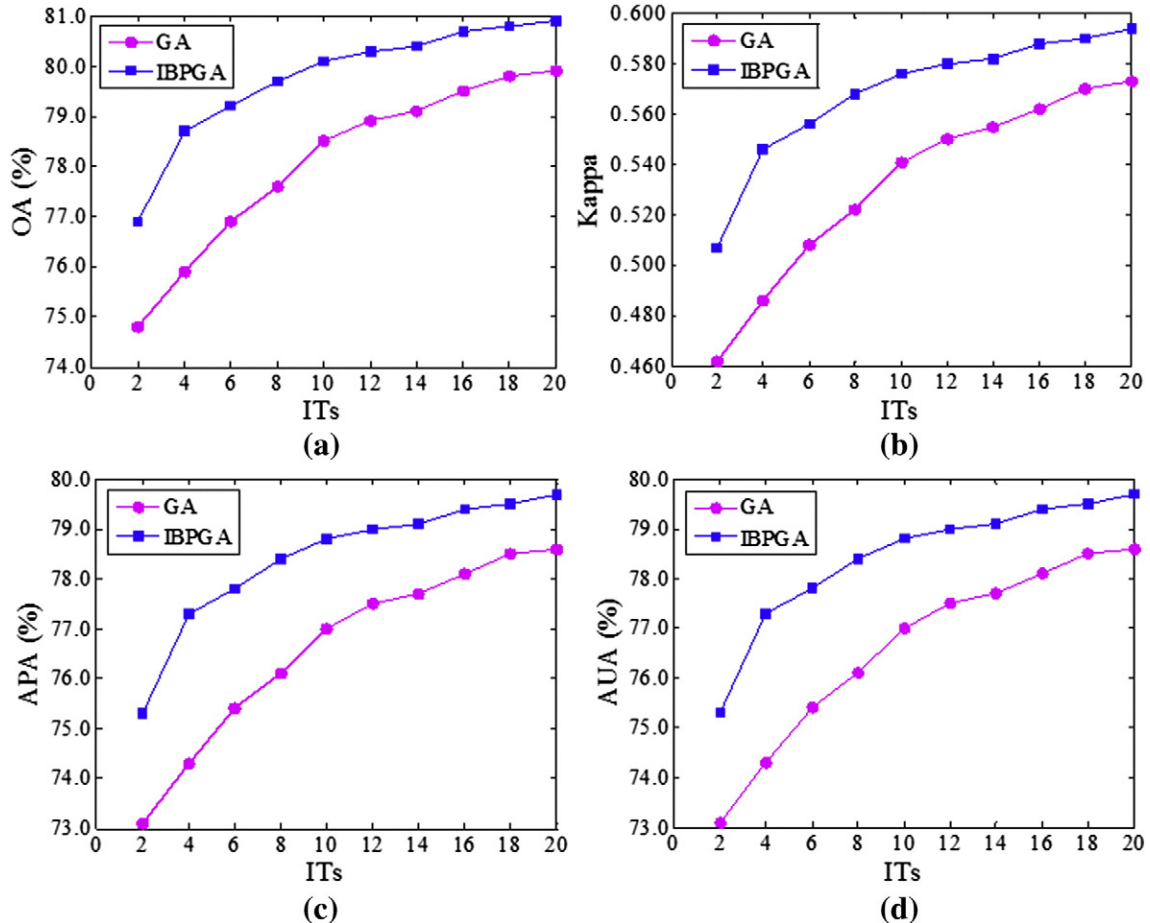

Fig. 11. Convergence performance of GA-SMWI and IBPGA-SMWI. (a) Convergence performance related to OA. (b) Convergence performance related to Kappa. (c) Convergence performance related to APA. (d) Convergence performance related to AUA.

similar to the inundation reference images. IBPGA-SMWI obtained the most satisfactory results among the four SMWI methods in the two wetlands. It mapped the inundation more continuously and smoothly than other SMWI methods.

Table 3 shows the quantitative comparisons of the four SMWI methods in the two study areas. We compared the results using measures of overall accuracy (OA), Kappa coefficient, average producer's accuracy (APA) and average user's accuracy (AUA) (Foody, 2002; Liu, Frazier, & Kumar, 2007). All pure pixels in the inundation fraction images were excluded from calculations. From Table 3, we can see that IBPGA-SMWI exhibits the highest OA, Kappa, APA and AUA in the two study areas. For example, the OA values of SAM-SMWI, BP-SMWI, GA-SMWI and IBPGA-SMWI are 72.4%, 75.4%, 78.5%, and 80.1% in the study area 1, respectively. The OA values of SAM-SMWI, BP-SMWI, GA-SMWI and IBPGA-SMWI are 74.1%, 77.8%, 79.3%, and 81.0% in the study area 2, respectively. In the process of SMWI, IBPGA-SMWI searches for the most likely distributions of sub-pixels within each mixed pixel and obtains the SMWI results in a pixel-by-pixel fashion regardless of the total number of pixels processed. Therefore, IBPGA-SMWI can obtain satisfactory results in both small and large areas.

We further compared GA-SMWI with IBPGA-SMWI in terms of the convergence performance in the study area 1 because both are based on GA which is a stochastic optimization algorithm. The results are shown in Table 4 and Fig. 11 where ITs represent iterative times. Compared with GA-SMWI, IBPGA-SMWI has better convergence performance in SMWI accuracy and convergence speed. For example, the OA value of GA-SMWI is 79.9% at the 20th iteration while the OA value of IBPGA-SMWI is 80.1% only at the 10th iteration.

4.2. Sensitivity analysis of IBPGA-SMWI

Crossover and mutation are the key operations of GA (Faghihi et al., 2014; Van Coillie et al., 2007). Compared with standard GA, BP crossover is a characteristic operation of IBPGA. Therefore, the sensitivity analysis of IBPGA-SMWI in relation to standard crossover rate (SCR), BP crossover rate (BPCR) and mutation rate (MR) was carried out to evaluate their roles in performance. The ETM + image of the study area 1 (in Fig. 8(a)) and the TM image of the study area 2 (in the red rectangle area in Fig. 8(d)) were tested using different parameter values. To analyze the IBPGA-SMWI sensitivity in relation to SCR, BPCR and MR, other parameters were kept the same as those in the case study. SCR, BPCR and MR values were assumed as: {0.1, 0.3, 0.5, 0.7, 0.9}.

Sensitivity of IBPGA-SMWI is shown in Table 5 and Fig. 12. It can be observed that IBPGA-SMWI obtained high SMWI accuracy when SCR, BPCR and MR were set to different values. The higher the SCR and MR values, the higher the SMWI accuracy. For example, OA value increases from 79.7% to 80.2% when SCR value is from 0.1 to 0.9 in the study area 1. The values of Kappa, APA and AUA have the similar increasing trend as that of OA. That is because the higher the SCR and MR values, the more chances for individuals to participate in the standard crossover and mutation process. More new individuals will be produced which can increase the diversity of the population and be in favor of getting the optimal solutions. With the increase of the BPCR value, SMWI accuracy first increases to the maximum value and then decreases. For example, the OA value first increases from 79.5% to 80.1% when the BPCR value is from 0.1 to 0.5 in the study area 1. Then the OA value decreases from 80.1% to 79.9% when the BPCR value is from 0.5 to 0.9. The OA value reaches a maximum when the BPCR value is 0.5. That is
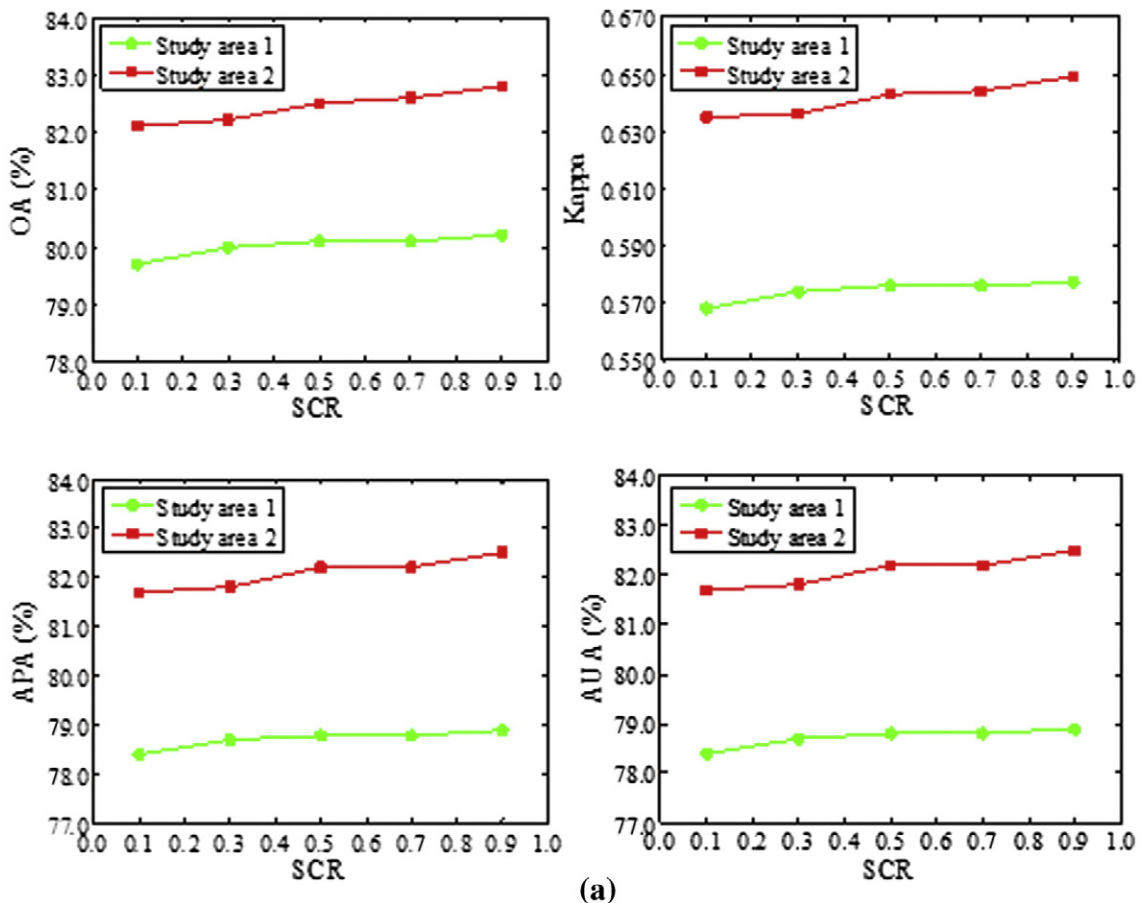

Fig. 12. Sensitivity of IBPGA-SMWI. (a) Sensitivity in relation to SCR. (b) Sensitivity in relation to BPCR. (c) Sensitivity in relation to MR.
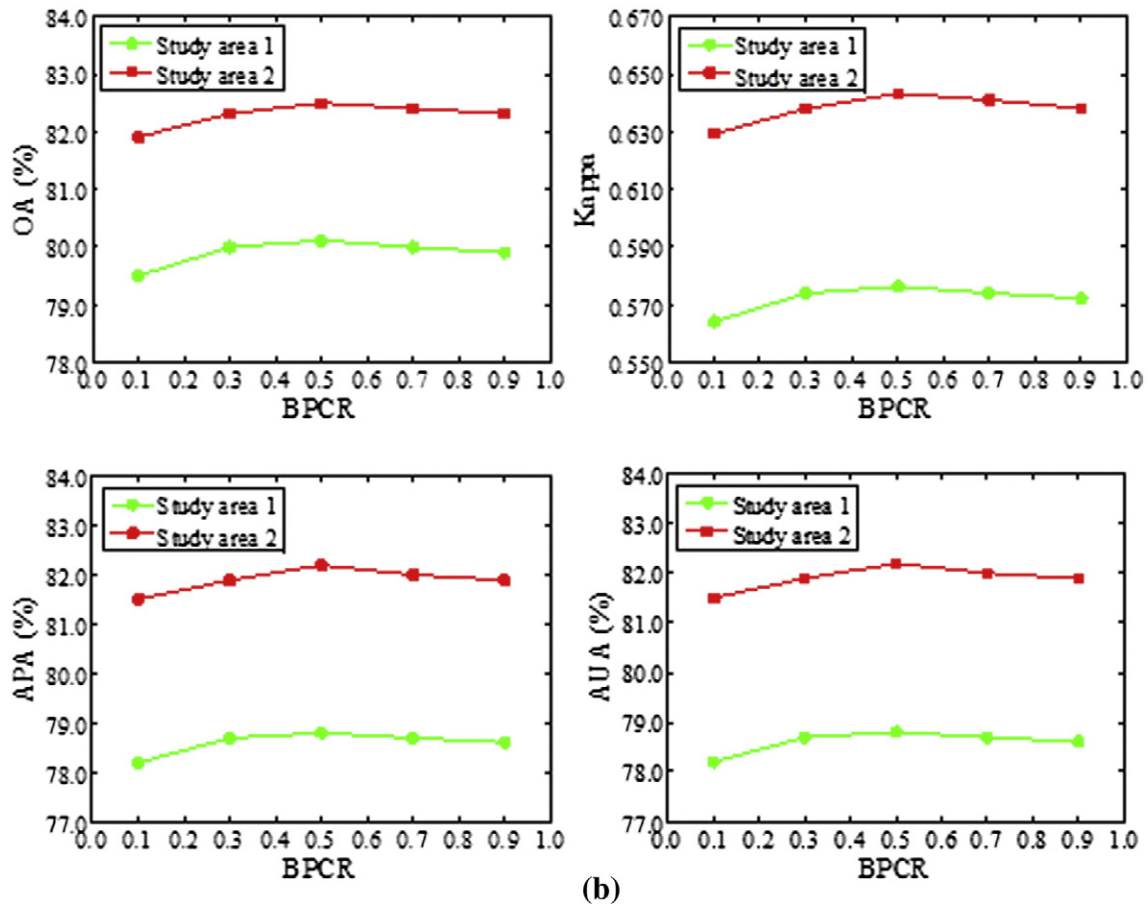
(b)

Fig. 12 (*continued*).

because high BPCR value will increase the possibility of individuals' involvement in the BP crossover process. As prior knowledge, the results of BP can be integrated into the new individuals by BP crossover, which will improve the SMWI accuracy. However, if BPCR value is too large, new individuals will be much alike and the diversity of the population will decrease.

4.3. Discussion of a real world situation

Wetland inundation has spatio-temporal distributions. In order to apply and evaluate IBPGA-SMWI in a real world situation, two multispectral remote sensing images with different resolutions at the same time in the same study area are needed. One image is a low resolution image from which the inundation fraction image can be derived. Another image is a high resolution image from which the inundation reference image can be obtained. Although there have been so many remote sensing satellites flying in the key, it is still a difficult job to have valid image data from two different satellite systems at a close enough time in a specific study area. However, if it is the case that those image data are from two satellite systems, there should be no technical obstacles to apply the methodology to those image data. The processing procedure may have to be slightly tuned to coordinate those data. Take 30 m Landsat ETM + multispectral image and 4 m IKONOS multispectral image for example. First, a geometric registration on the IKONOS image is needed to be implemented so that each corrected pixel of the output IKONOS image has the same coordinate as the ETM + image. Second, the resolution of the ETM + image is needed to be resampled to 28 m, which is seven times the resolution of the IKONOS image. Third, the inundation fraction image at 28 m resolution can be derived from the 28 m ETM + image

using the least squares linear spectral mixture analysis method (Heinz & Chang, 2001) by ENVI remote sensing image processing software (Exelis Visual Information Solutions, Inc., 2015). Fourth, IBPGA-SMWI can be applied to obtain a 4 m SMWI result from the 28 m fraction image. Fifth, supervised image classification methods, such as neural networks, can be used to classify the IKONOS image into an inundation reference image with two classes representing inundation and non-inundation respectively. Finally, the SMWI result can be evaluated using the similar visual and quantitative comparisons with the inundation reference image.

IBPGA-SMWI is likely to have a lower accuracy if the coarse and fine resolution images come from different satellite systems. The following elements may potentially compromise the accuracy of IBPGA-SMWI: a) the temporal mismatching between the coarse resolution image and the fine resolution image, in particular in a wetland with a dynamic hydrological condition. Any inundation fluctuations during the time gap may undermine the accuracy; b) the accuracy of implementing geometric registration between those two image data from different satellites; c) any other possible mismatching issues between two different satellite platforms.

5. Conclusions

In this study, a new integration method called IBPGA-SMWI was proposed to achieve improved performance in mapping wetland inundation at a sub-pixel scale from multispectral remote sensing imagery. The IBPGA-SMWI algorithm was developed, including the fitness function and integration search strategy. We assessed the results of IBPGA-SMWI using Landsat TM/ETM + imagery from the Poyanghu wetland in China
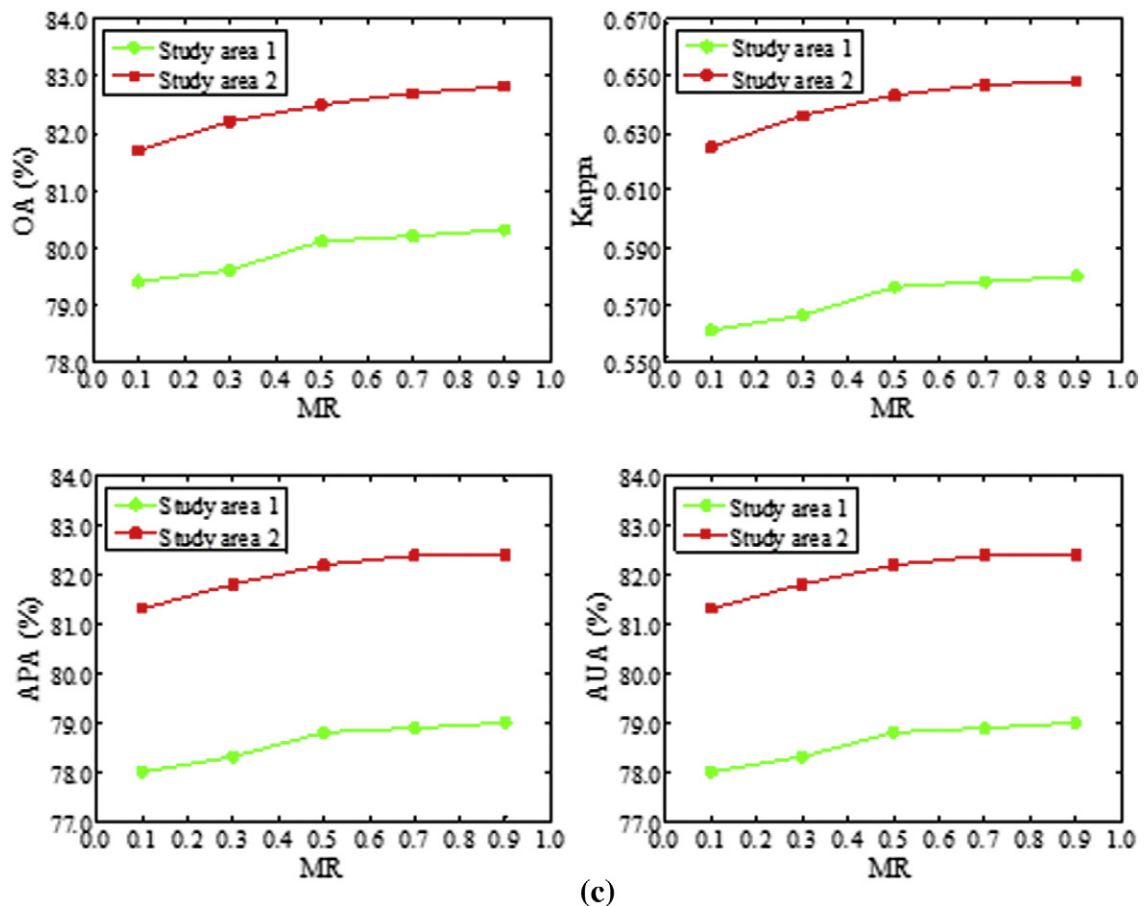
Fig. 12 (*continued*).

and the Macquarie Marshes in Australia. The sensitivity analysis of IBPGA-SMWI in relation to SCR, BPCR and MR was also carried out to discuss the algorithm performance.

IBPGA-SMWI mapped the inundation more continuously and smoothly than other three SMWI methods in the two wetlands. Besides visual comparisons, IBPGA-SMWI consistently achieves more accurate results in terms of quantitative evaluations using measures of OA, Kappa, APA and AUA. Both GA-SMWI and IBPGA-SMWI are based on GA which is a stochastic optimization algorithm. Compared with GA-SMWI, IBPGA-SMWI not only improves the accuracy of SMWI, but also accelerates the convergence speed of the algorithm. IBPGA-SMWI can obtain satisfactory results in both small and large areas. In the process of SMWI, IBPGA-SMWI searches for the most likely distributions of sub-pixels within each mixed pixel and obtains the SMWI results in a pixel-by-pixel fashion regardless of the total number of pixels processed. Therefore, the assumption that coupled with BP, GA has the potential to be applied to SMWI has proved to be valid.

The study of wetland inundation has an important significance to the environment and associated plant and animal life. We hope that the results of this study will enhance the application of median-low resolution remote sensing imagery in wetland inundation mapping and monitoring, and thereby benefit the studies of wetland environment.

References

Acosta-Gonzalez, E., & Fernandez-Rodriguez, F. (2014). Forecasting financial failure of firms via genetic algorithms. *Computational Economics, 43*, 133–157.

Aplin, P., & Atkinson, P. M. (2001). Sub-pixel land cover mapping for per-field classification. *International Journal of Remote Sensing, 22*, 2853–2858.

Ardila, J. P., Tolpekin, V. A., Bijker, W., & Stein, A. (2011). Markov-random-field-based super-resolution mapping for identification of urban trees in VHR images. *ISPRS Journal of Photogrammetry and Remote Sensing, 66*, 762–775.

Atkinson, P. M. (1997). Mapping sub-pixel boundaries from remotely sensed images. *Innovations in GIS, 4*, 166–180.

Atkinson, P. M. (2005). Sub-pixel target mapping from soft-classified, remotely sensed imagery. *Photogrammetric Engineering and Remote Sensing, 71*, 839–846.

Chen, Y., Barrett, D., Liu, R., Gao, L., Zhou, M., Renzullo, L., et al. (2014a). A spatial framework for regional-scale flooding risk assessment. *7th International Congress on Environmental Modeling and Software, San Diego, USA.*

Chen, Y., Cuddy, S. M., Wang, B., & Merrin, L. (2011). Linking inundation timing and extent to ecological response models using the Murray–Darling Basin Floodplain Inundation Model (MDB-FIM). *19th International Congress on Modelling and Simulation, Perth, Australia.*

Chen, Y., Huang, C., Ticehurst, C., Merrin, L., & Thew, P. (2013). An evaluation of MODIS daily and 8-day composite products for floodplain and wetland inundation mapping. *Wetlands, 33*, 823–835.

Chen, Y., Wang, B., Pollino, C., Cuddy, S., Merrin, L., & Huang, C. (2014b). Estimate of flood inundation and retention on wetlands using remote sensing and GIS. *Ecohydrology, 7*, 1412–1420.

Cheng, Q., Varshney, P. K., & Arora, M. K. (2006). Logistic regression for feature selection and soft classification of remote sensing data. *IEEE Geoscience and Remote Sensing Letters, 3*, 491–494.

Delavar, M. R., Hajiaghaei-Keshteli, M., & Molla-Alizadeh-Zavardehi, S. (2010). Genetic algorithms for coordinated scheduling of production and air transportation. *Expert Systems with Applications, 37*, 8255–8266.

Exelis Visual Information Solutions, Inc. (2015). ENVI online tutorials. http://www.exelisvis.com/ProductsServices/ENVIProducts/ENVI.aspx

Faghihi, V., Reinschmidt, K. F., & Kang, J. H. (2014). Construction scheduling using genetic algorithm based on building information model. *Expert Systems with Applications, 41*, 7565–7578.

Foody, G. M. (2002). Status of land cover classification accuracy assessment. *Remote Sensing of Environment, 80*, 185–201.

Heinz, D. C., & Chang, C. (2001). Fully constrained least squares linear spectral mixture analysis method for material quantification in hyperspectral imagery. *IEEE Transactions on Geoscience and Remote Sensing, 39*, 529–545.

Hu, T., Xu, J., Zhang, D., Wang, J., & Zhang, Y. (2013). Hard and soft classification method of multi-spectral remote sensing image based on adaptive thresholds. *Spectroscopy and Spectral Analysis, 33*, 1038–1042.

Huang, C., Chen, Y., & Wu, J. (2014a). DEM-based modification of pixel-swapping algorithm for enhancing floodplain inundation mapping. *International Journal of Remote Sensing, 35*, 365–381.

Huang, C., Chen, Y., & Wu, J. (2014b). Mapping spatio-temporal flood inundation dynamics at large river basin scale using time-series flow data and MODIS imagery. *International Journal of Applied Earth Observation and Geoinformation, 26*, 350–362.

Huang, C., Chen, Y., Wu, J., Chen, Z., Li, L., Liu, R., et al. (2014c). Integration of remotely sensed inundation extent and high-precision topographic data for mapping inundation depth. *3rd International Conference on Agro-Geoinformatics, Beijing, China*.

Huang, C., Chen, Y., Wu, J., & Yu, J. (2012). Detecting floodplain inundation frequency using MODIS time-series imagery. *1st International Conference on Agro-Geoinformatics, Shanghai, China*.

Huang, C., Peng, Y., Lang, M., Yeo, I., & McCarty, G. (2014d). Wetland inundation mapping and change monitoring using Landsat and airborne LiDAR data. *Remote Sensing of Environment, 141*, 231–242.

Kanemura, A., Maeda, S., & Ishii, S. (2009). Superresolution with compound Markov random fields via the variational EM algorithm. *Neural Networks, 22*, 1025–1034.

Li, L., Chen, Y., Yu, X., Liu, R., & Huang, C. (2015). Sub-pixel flood inundation mapping from multispectral remotely sensed images based on discrete particle swarm optimization. *ISPRS Journal of Photogrammetry and Remote Sensing, 101*, 10–21.

Li, X., Du, Y., & Ling, F. (2014a). Super-resolution mapping of forests with bitemporal different spatial resolution images based on the spatial–temporal Markov random field. *IEEE Journal of Selected Topics in Applied Earth Observations and Remote Sensing, 7*, 29–39.

Li, X., Ling, F., Du, Y., Feng, Q., & Zhang, Y. (2014b). A spatial–temporal Hopfield neural network approach for super-resolution land cover mapping with multi-temporal different resolution remotely sensed images. *ISPRS Journal of Photogrammetry and Remote Sensing, 93*, 76–87.

Liu, C., Frazier, P., & Kumar, L. (2007). Comparative assessment of the measures of thematic classification accuracy. *Remote Sensing of Environment, 107*, 606–616.

Mahmoudabadi, A., & Tavakkoli-Moghaddam, R. (2011). The use of a genetic algorithm for clustering the weighing station performance in transportation — A case study. *Expert Systems with Applications, 38*, 11744–11750.

Marti-Cardona, B., Dolz-Ripolles, J., & Lopez-Martinez, C. (2013). Wetland inundation monitoring by the synergistic use of ENVISAT/ASAR imagery and ancilliary spatial data. *Remote Sensing of Environment, 139*, 171–184.

Melin, F., Zibordi, G., & Berthon, J. (2012). Uncertainties in remote sensing reflectance from MODIS-Terra. *IEEE Geoscience and Remote Sensing Letters, 9*, 432–436.

Mertens, K. C., De Baets, B., Verbeke, L. P. C., & De Wulf, R. R. (2006). A sub-pixel mapping algorithm based on sub-pixel/pixel spatial attraction models. *International Journal of Remote Sensing, 27*, 3293–3310.

Mertens, K. C., Verbeke, L. P. C., Westra, T., & De Wulf, R. R. (2004). Sub-pixel mapping and sub-pixel sharpening using neural network predicted wavelet coefficients. *Remote Sensing of Environment, 91*, 225–236.

Mesbah, M., Sarvi, M., & Currie, G. (2011). Optimization of transit priority in the transportation network using a genetic algorithm. *IEEE Transactions on Intelligent Transportation Systems, 12*, 908–919.

Oyana, T. J., & Dai, D. (2010). Automatic cluster identification for environmental applications using the self-organizing maps and a new genetic algorithm. *Geocarto International, 25*, 53–69.

Ozturk, H. K., & Ceylan, H. (2005). Forecasting total and industrial sector electricity demand based on genetic algorithm approach: Turkey case study. *International Journal of Energy Research, 29*, 829–840.

Paola, J. D., & Schowengerdt, R. A. (1995). A detailed comparison of backpropagation neural-network and maximum-likelihood classifiers for urban land-use classification. *IEEE Transactions on Geoscience and Remote Sensing, 33*, 981–996.

Preechakul, C., & Kheawhom, S. (2009). Modified genetic algorithm with sampling techniques for chemical engineering optimization. *Journal of Industrial and Engineering Chemistry, 15*, 110–118.

Qian, F., Sun, F., Zhong, W., & Luo, N. (2013). Dynamic optimization of chemical engineering problems using a control vector parameterization method with an iterative genetic algorithm. *Engineering Optimization, 45*, 1129–1146.

Quang, M. N., Atkinson, P. M., & Lewis, H. G. (2011). Super-resolution mapping using Hopfield neural network with panchromatic imagery. *International Journal of Remote Sensing, 32*, 6149–6176.

Ramsar (2009). What are wetlands? October 8, 2009. http://archive.ramsar.org/cda/es/ramsar-about-faqs-what-are-wetlands/main/ramsar/1-36-37%5E7713_4000_2__

Ramsar (2014). The list of wetlands of international importance. September 11, 2014. http://www.ramsar.org/sites/default/files/documents/library/sitelist.pdf

Shad, R., & Shad, A. (2012). Uncertain spatial reasoning of environmental risks in GIS using genetic learning algorithms. *Environmental Monitoring and Assessment, 184*, 6307–6323.

Song, K., Lu, D., Li, L., Li, S., Wang, Z., & Du, J. (2012). Remote sensing of chlorophyll-a concentration for drinking water source using genetic algorithms (GA)–partial least square (PLS) modeling. *Ecological Informatics, 10*, 25–36.

Suksonghong, K., Boonlong, K., & Goh, K. (2014). Multi-objective genetic algorithms for solving portfolio optimization problems in the electricity market. *International Journal of Electrical Power & Energy Systems, 58*, 150–159.

Ticehurst, C., Chen, Y., Karim, F., & Dushmanta, D. (2013). Using MODIS for mapping flood events for use in hydrological and hydrodynamic models: Experiences so far. *20th International Congress on Modelling and Simulation, Adelaide, Australia*.

Tong, X., Zhang, X., & Liu, M. (2010). Detection of urban sprawl using a genetic algorithm-evolved artificial neural network classification in remote sensing: A case study in Jiading and Putuo districts of Shanghai, China. *International Journal of Remote Sensing, 31*, 1485–1504.

Van Coillie, F. M. B., Verbeke, L. P. C., & De Wulf, R. R. (2007). Feature selection by genetic algorithms in object-based classification of IKONOS imagery for forest mapping in Flanders, Belgium. *Remote Sensing of Environment, 110*, 476–487.

Vazhayil, J. P., & Balasubramanian, R. (2014). Optimization of India's electricity generation portfolio using intelligent Pareto-search genetic algorithm. *International Journal of Electrical Power & Energy Systems, 55*, 13–20.

Verhoeye, J., & De Wulf, R. (2002). Land cover mapping at sub-pixel scales using linear optimization techniques. *Remote Sensing of Environment, 79*, 96–104.

Wiesinger, J., Sornette, D., & Satinover, J. (2013). Reverse engineering financial markets with majority and minority games using genetic algorithms. *Computational Economics, 41*, 475–492.

Wu, Z., Yi, L., & Zhang, G. (2009). Uncertainty analysis of object location in multi-source remote sensing imagery classification. *International Journal of Remote Sensing, 30*, 5473–5487.

Xu, H. (2006). Modification of normalised difference water index (NDWI) to enhance open water features in remotely sensed imagery. *International Journal of Remote Sensing, 27*, 3025–3033.

Xu, M., Watanachaturaporn, P., Varshney, P. K., & Arora, M. K. (2005). Decision tree regression for soft classification of remote sensing data. *Remote Sensing of Environment, 97*, 322–336.

Yang, M. (2007). A genetic algorithm (GA) based automated classifier for remote sensing imagery. *Canadian Journal of Remote Sensing, 33*, 203–213.

Yang, C., & Yan, X. (2011). A fuzzy-based adaptive genetic algorithm and its case study in chemical engineering. *Chinese Journal of Chemical Engineering, 19*, 299–307.

Yang, X., Yang, Z., Shen, Z., & Li, J. (2006). A grey-encoded hybrid accelerating genetic algorithm for parameter optimisation of environmental models. *International Journal of Environment and Pollution, 28*, 239–252.

Zhang, L., Wu, K., Zhong, Y., & Li, P. (2008). A new sub-pixel mapping algorithm based on a BP neural network with an observation model. *Neurocomputing, 71*, 2046–2054.

Zhao, X., Stein, A., & Chen, X. (2011). Monitoring the dynamics of wetland inundation by random sets on multi-temporal images. *Remote Sensing of Environment, 115*, 2390–2401.